QUARTERLY JOURNAL OF THE ROYAL METEOROLOGICAL SOCIETY
Q. J. R. Meteorol. Soc. **134**: 583–593 (2008)
Published online in Wiley InterScience
(www.interscience.wiley.com) DOI: 10.1002/qj.237

Some dynamical aspects of tropical cyclone concentric eyewalls

Christopher M. Rozoff,[a]* Wayne H. Schubert[b] and James P. Kossin[a]
[a] *University of Wisconsin-Madison, USA*
[b] *Colorado State University, USA*

ABSTRACT: The intensification of tropical cyclones is often interrupted by an eyewall replacement cycle, a process in which an outer eyewall forms, contracts, and replaces an inner eyewall. The radial distributions of inertial stability and diabatic heating change during such events, impacting the transverse circulation. To examine the effects of such changes, an analytical solution of the transverse circulation equation associated with a balanced vortex model is derived using a parameterization that distinguishes five radial regions subdividing the domain by each region's values of inertial stability and diabatic heating. These regions define the eye, inner eyewall, moat, outer eyewall, and far-field. In mature concentric eyewall situations, the solutions do not support the hypothesis that the inner eyewall collapses as a direct result of subsidence from the outer eyewall. However, the results suggest subsidence and warming temperatures in the moat are governed by enhanced inertial stability associated with a strengthening outer eyewall. The model solutions also illustrate how the diabatic heating in the inner eyewall, imbedded in a region of high inertial stability, induces larger temperature tendencies than the diabatic heating in the outer eyewall, which borders the far-field region of low inertial stability. Thus, as the inner eyewall dies, the storm temporarily loses its ability to produce an intense, localized warm region. This ability is restored during the contraction and intensification of the outer eyewall. These results provide a partial dynamical explanation of how an eyewall replacement cycle can act as a temporary brake on tropical cyclone intensification. Copyright © 2008 Royal Meteorological Society

KEY WORDS hurricane; eyewall replacement cycle; moat

Received 27 September 2007; Revised 5 February 2008; Accepted 20 February 2008

1. Introduction

An important prerequisite to improved forecasting of tropical cyclone intensity is a better understanding of the concentric eyewall phenomenon. Eyewall replacement cycles are often associated with large and rapid intensity fluctuations. An example of this behavior was observed in hurricane *Allen* (1980), which underwent repeated swings in its minimum central pressure of ~50 hPa (Willoughby *et al.*, 1982) within 12- to 24-hour periods. Such rapid intensification poses a particularly dangerous situation when a tropical cyclone is approaching land. This occurred in hurricane *Andrew* (1992) while making landfall near Homestead, Florida. As *Andrew* approached southern Florida, it weakened as an outer eyewall formed around the primary eyewall. Just prior to moving onshore, however, the outer eyewall contracted and replaced the primary eyewall, causing a rapid intensification that was not well forecast (Willoughby and Black, 1996). In the 18-hour period prior to landfall, *Andrew* intensified from 57 m s^{-1} to 77 m s^{-1}, resulting in an unexpectedly high loss of life and property. More generally, even as a tropical cyclone weakens during the formation of an outer eyewall, the width of damaging winds can expand and thereby offset some of the societal benefits of a weakened inner eyewall.

A more recent example of a storm with concentric eyewalls was hurricane *Frances* (2004), which reached category 4 on the Saffir–Simpson scale. *Frances* arose from a tropical wave that moved off the western coast of Africa on 21 August. The system was classified as a tropical depression at 0000 UTC on 25 August. The subsequent intensity timeline for *Frances* is shown in Figure 1, which has been adapted from the National Hurricane Center's Best Track data archive. By 1800 UTC on 28 August, the storm had attained an estimated maximum surface wind speed of 60 m s^{-1} and minimum sea-level pressure of 948 hPa. Then, as *Frances* passed to the north of the Leeward and Virgin Islands, an eyewall replacement cycle commenced, with concentric eyewalls clearly evident in NOAA WP-3D aircraft radar and wind observations. During this eyewall replacement cycle, the maximum surface wind speed decreased to 51 m s^{-1} and the minimum surface pressure rose to 958 hPa. As the initial, inner eyewall diminished and the outer eyewall contracted, the storm began its course toward its highest sustained surface wind speed of 64 m s^{-1} and lowest sea-level pressure of 937 hPa. After 2 September, an

* Correspondence to: Christopher M. Rozoff, Space Science and Engineering Center, University of Wisconsin-Madison, Madison, WI 53718. E-mail: chris.rozoff@ssec.wisc.edu

Copyright © 2008 Royal Meteorological Society

environment of increasing vertical wind shear impeded the storm from achieving its previous maximum intensity again. The storm made landfall on the central, eastern coast of Florida around 0430 UTC on 5 September as a category 2 hurricane.

Figure 2 shows radar reflectivity and radial profiles of tangential wind, temperature, and dewpoint temperature collected from a NOAA WP-3D aircraft in Frances during a 3.5 h interval on 30 August 2004. During this time period, *Frances* possessed concentric eyewalls, with a 100 km diameter outer eyewall and a 30 km diameter inner eyewall that became increasingly asymmetric in time (Figure 2(a,c,e)). A consistent asymmetric structure also occurred in both the tangential wind profiles (Figure 2(b,d,f)) and the moat between the concentric eyewalls. Dewpoint depressions as large as 6 °C appeared

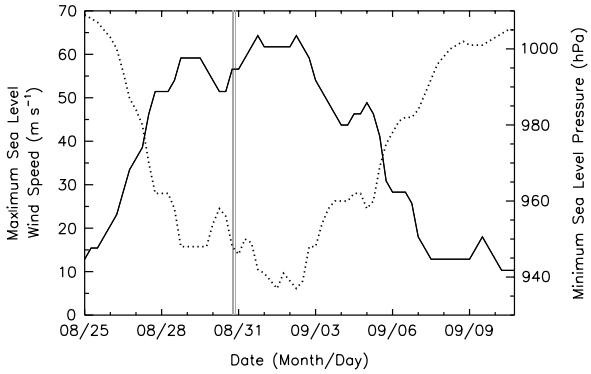

Figure 1. National Hurricane Center Best Track intensity for hurricane *Frances* (2004) throughout the storm's lifecycle: maximum surface wind speed (m s^{-1}, solid) and minimum sea-level central pressure (hPa, dotted). Vertical lines depict the times at which the flight-level data utilized in this paper were obtained.

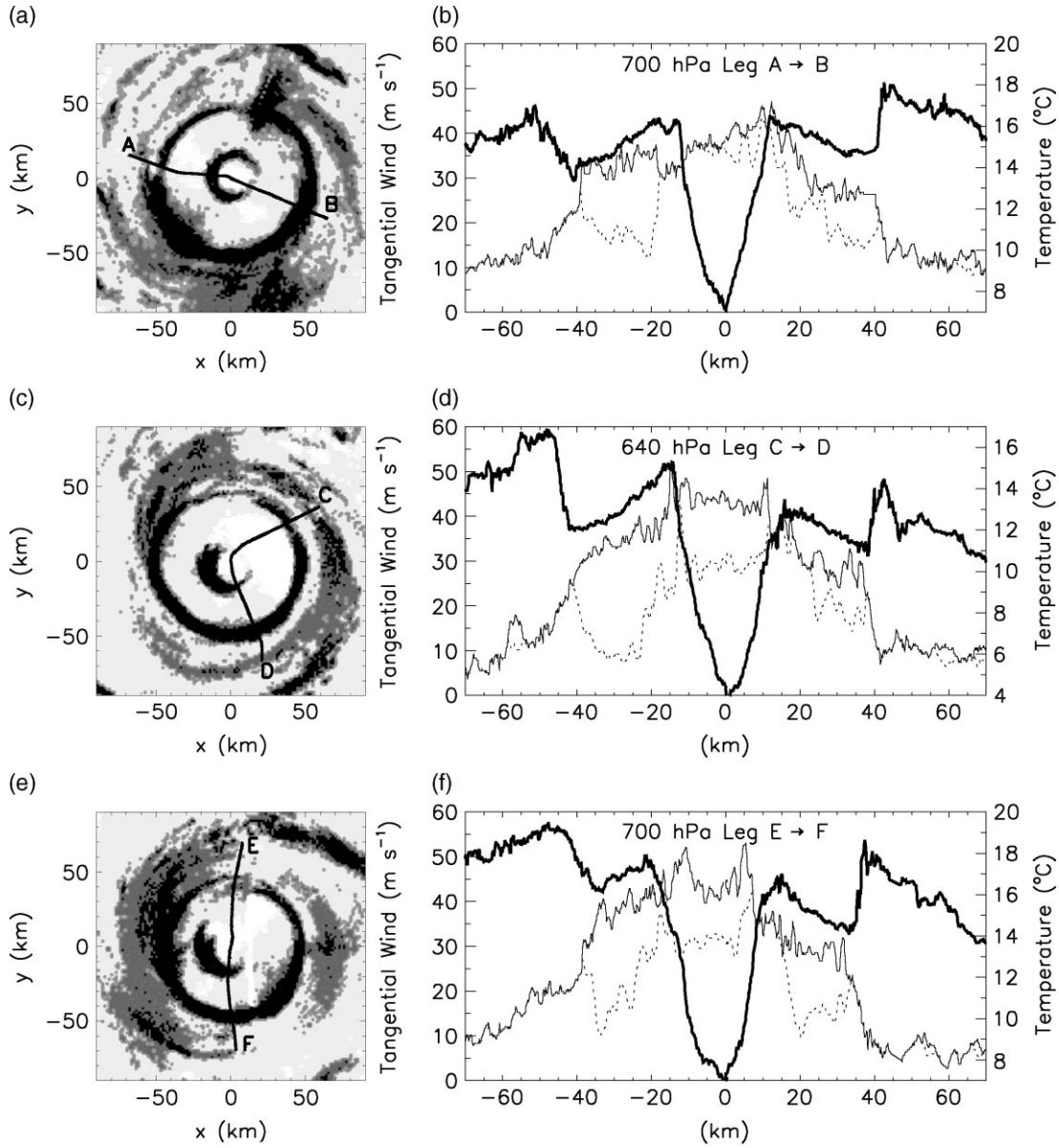

Figure 2. Radar reflectivity and radial profiles of flight-level tangential wind (m s^{-1}, bold solid), temperature (°C, thin solid), and dewpoint temperature (°C, dashed) for hurricane *Frances* for (a,b) 1800–1826 UTC (leg A→B), (c,d) 1919–1947 UTC (leg C→D), and (e,f) 2104–2129 UTC (leg E→F) on 30 August 2004. Data obtained courtesy of NOAA/HRD.

Copyright © 2008 Royal Meteorological Society

DOI: 10.1002/qj

in the northeast sector at 640 hPa (Figure 2(d)), suggestive of enhanced subsidence there. The most striking aspects of these observations are the high temperatures and large dewpoint depressions that occur inside the radius of the outer eyewall. Within the primary eyewall, particularly elevated temperatures are observed. In fact, the leg E→F radial profile reveals a warm ring structure just inside the inner eyewall.

Eyewall replacement cycles, similar to those observed in *Frances*, are well documented (Willoughby *et al.*, 1982; Hawkins *et al.*, 2006), but many fundamental aspects of eyewall cycles are not fully understood. While high-resolution mesoscale models show promise in capturing eyewall cycles and their attendant, rapid intensity changes (Houze *et al.*, 2006), the formation of secondary eyewalls remains a topic of active research (e.g. Kuo *et al.*, 2004, 2008; Terwey and Montgomery, 2008). Nonetheless, there are unexplored aspects of the balanced, axisymmetric dynamics of mature concentric eyewall configurations that still deserve attention.

Based on Eliassen's (1951) transverse circulation equation, Shapiro and Willoughby (1982) argued that eyewall contraction occurs inside the radius of maximum wind due to a large gradient in inertial stability there. In particular, the local tendency of tangential winds is modulated by the relative positions of the convective updraughts (i.e. heat sources) and the radius of maximum wind (RMW). Eyewall contraction (expansion) occurs when convective updraughts are located inside (outside) the RMW. The RMW contracts (expands) because the tangential wind tendency has greatest positive value inside (outside) the RMW. Further exploring Eliassen's transverse circulation equation and incorporating observations of concentric eyewalls, Willoughby *et al.* (1982) found that the situation of two concentric eyewalls creates hostile conditions for the inner eyewall, since a component of low-level outflow from the outer ring decreases inflow at radii within the outer ring. Similarly, a region of negative tangential wind tendency appears at radii well within the outer ring. Using an axisymmetric, non-hydrostatic model, Hausman (2001) simulated a tropical cyclone with eyewall replacement cycles. Through an entropy budget in the boundary layer, Hausman determined that downward advection of low-entropy air exceeds the upward turbulent flux of high-entropy air from the sea surface as a simulated secondary eyewall forms. At the same time, the secondary eyewall decreases the low-level, inward advection of angular momentum inside the secondary eyewall. Hence, the presence of an outer eyewall weakens the inner eyewall in axisymmetric studies. Nonetheless, more insights into details of the balanced dynamics occurring in eyewall replacement cycles can be gained using Eliassen's transverse circulation equation.

This paper is organized in the following way. First, the balanced vortex model is presented in Section 2. In Section 3 idealized solutions of the transverse circulation equation are derived. With the aid of observational data and our idealized solutions, Section 4 quantitatively addresses mechanisms that suppress the inner eyewall during an eyewall replacement cycle. Along these same lines, the decreasing ability of the storm to maintain a strong, centralized warm core during an eyewall replacement cycle is investigated in Section 5. In Section 6, we consider changes in the transverse circulation during a hypothetical eyewall replacement cycle in our balanced vortex framework. These results suggest that subsidence in the moat rapidly increases as a secondary eyewall forms. Finally a summary of the results and conclusions is presented in Section 7.

2. Balanced vortex model

Following Schubert *et al.* (2007), we consider inviscid, axisymmetric, quasi-static, quasi-gradient motions of a stratified, compressible atmosphere on an f-plane. As the vertical coordinate we use $z = H\ln(p_0/p)$, where $H = RT_0/g$ is the constant scale height, and where $p_0 =$ 100 kPa and $T_0 = 300$ K are constant reference values of pressure and temperature. The governing equations for this balanced vortex model are

$$\left(f+\frac{v}{r}\right)v=\frac{\partial\phi}{\partial r},\qquad \frac{\mathrm{D}v}{\mathrm{D}t}+\left(f+\frac{v}{r}\right)u=0,$$
$$\frac{\partial\phi}{\partial z}=\frac{g}{T_0}T,\qquad \frac{\partial(ru)}{r\partial r}+\frac{\partial w}{\partial z}-\frac{w}{H}=0,$$
$$\frac{\mathrm{D}T}{\mathrm{D}t}+\frac{RT}{c_pH}w=\frac{Q}{c_p},\quad (1)$$

where u and v are the radial and azimuthal components of velocity, $w = \mathrm{D}z/\mathrm{D}t$ the 'log-pressure vertical velocity', ϕ the geopotential, T the temperature, f the constant Coriolis parameter, Q the diabatic heating, and $\mathrm{D}/\mathrm{D}t = \partial/\partial t + u(\partial/\partial r) + w(\partial/\partial z)$ the material derivative.

The balanced vortex model given in (1) may be transformed to a set of four diagnostic equations and one prognostic equation. Because of the continuity equation, the transverse circulation (u, w) can be expressed in terms of the streamfunction ψ such that

$$\mathrm{e}^{-z/H}u=-\frac{\partial\psi}{\partial z}\quad\text{and}\quad \mathrm{e}^{-z/H}w=\frac{\partial(r\psi)}{r\partial r}.$$

Taking the local time derivative of the thermal wind equation

$$\left(f+\frac{2v}{r}\right)\frac{\partial v}{\partial z}=\frac{g}{T_0}\frac{\partial T}{\partial r},$$

derived from (1) allows for the elimination of the local time derivatives in the tangential wind and thermodynamic equations. The resulting diagnostic equation for ψ is the transverse circulation equation (Eliassen, 1951):

$$\frac{\partial}{\partial r}\left\{A\frac{\partial(r\psi)}{r\partial r}+B\frac{\partial\psi}{\partial z}\right\}+\frac{\partial}{\partial z}\left\{B\frac{\partial(r\psi)}{r\partial r}+C\frac{\partial\psi}{\partial z}\right\}=\frac{g}{c_pT_0}\frac{\partial Q}{\partial r},\quad (2)$$

Copyright © 2008 Royal Meteorological Society

DOI: 10.1002/qj

where the static stability A, the baroclinity B, and the inertial stability C are defined by

$$A = \mathrm{e}^{z/H}\frac{g}{T_0}\left(\frac{\partial T}{\partial z} + \frac{RT}{c_p H}\right), \tag{3}$$

$$B = -\mathrm{e}^{z/H}\frac{g}{T_0}\frac{\partial T}{\partial r} = -\mathrm{e}^{z/H}\left(f + \frac{2v}{r}\right)\frac{\partial v}{\partial z}, \tag{4}$$

$$C = \mathrm{e}^{z/H}\left(f + \frac{2v}{r}\right)\left(f + \frac{\partial (rv)}{r\partial r}\right). \tag{5}$$

Only vortices with $AC - B^2 > 0$ everywhere are considered, which ensures that (2) is an elliptic equation. As for lateral boundary conditions on (2), we require that ψ vanish at $r = 0$ and that $r\psi \to 0$ as $r \to \infty$. The effects of boundary-layer friction and Ekman pumping could be incorporated through specification of ψ at the lower boundary of the free atmosphere (i.e. at the top of the Ekman layer). However, our focus here is on the transverse circulation induced by the diabatic heating, Q. Thus, we require that ψ vanish at both the bottom and top isobaric surfaces $z = 0, z_{\mathrm{T}}$.

Both of the prognostic equations in (1) have been used in the derivation of (2). Thus, if (2) is considered as one of the governing equations of the balanced vortex model, only one of the original prognostic equations need be used. Choosing to predict the mass field rather than the rotational wind field, we can write the thermodynamic equation as

$$\frac{\partial T}{\partial t} = \frac{Q}{c_p} - \frac{T_0}{g}\left(A\frac{\partial (r\psi)}{r\partial r} + B\frac{\partial \psi}{\partial z}\right). \tag{6}$$

In the following analysis we shall solve the elliptic equation (2) for the streamfunction ψ and then use this solution in (6) to obtain the implied tendency $\partial T/\partial t$.

3. Solutions of the transverse circulation equation

We now focus on the question of how the spatial variability of the inertial stability affects the transverse circulation when diabatic forcing is distributed into a double eyewall structure. To isolate this effect we consider a barotropic vortex ($B = 0$) in which the static stability is given by $A = e^{z/H}N^2$, where the Brunt-Väisälä frequency, N, is a constant. The inertial stability (5) can then be written in the form

$$C = \mathrm{e}^{z/H}\widehat{f}^2,$$

$$\text{where} \quad \widehat{f}(r) = \left[\left\{f + \frac{2v}{r}\right\}\left\{f + \frac{\partial (rv)}{r\partial r}\right\}\right]^{1/2}$$

is the 'effective Coriolis parameter'. It should be noted that real tropical cyclones, which possess warm cores, contain vertical shear of the tangential wind. Such a baroclinic vortex contains greater static stability at lower altitudes and less inertial stability at higher altitudes compared to the barotropic counterpart. As a result, the transverse circulation (u, w) and the associated temperature tendencies $\partial T/\partial t$ are shifted upward in altitude in the baroclinic situation. As shown in Schubert *et al.* (2007), numerical solutions of the transverse circulation for more realistic B show that the radial distributions of subsidence and associated temperature tendencies are similar between barotropic and baroclinic vortices. Numerical calculations verify the same characteristics for the five-region model. However, the essence of the following results relies on the radial distributions of diabatic heating and inertial stability. Consequently, the neglect of B is not a serious limitation for the purpose of this study, although further study of the impacts of variable B and N^2 may be of interest in future research endeavours.

The vertical structure of heating in convectively active, intense tropical cyclones (e.g. Rodgers *et al.*, 1998) typically exhibits a first vertical internal mode structure. Accordingly, we assume the diabatic heating $Q(r, z)$, the vertical velocity $w(r, z)$, the streamfunction $\psi(r, z)$, and the temperature tendency $\partial T(r, z)/\partial t$ have the separable forms

$$Q(r, z) = \widehat{Q}(r)\exp\left(\frac{z}{2H}\right)\sin\left(\frac{\pi z}{z_{\mathrm{T}}}\right),$$

$$w(r, z) = \widehat{w}(r)\exp\left(\frac{z}{2H}\right)\sin\left(\frac{\pi z}{z_{\mathrm{T}}}\right),$$

$$\psi(r, z) = \widehat{\psi}(r)\exp\left(\frac{-z}{2H}\right)\sin\left(\frac{\pi z}{z_{\mathrm{T}}}\right),$$

$$\frac{\partial T(r, z)}{\partial t} = \frac{\partial \widehat{T}(r)}{\partial t}\exp\left(\frac{z}{2H}\right)\sin\left(\frac{\pi z}{z_{\mathrm{T}}}\right),$$

so that (2) and (6) reduce to

$$r^2\frac{\mathrm{d}^2\widehat{\psi}}{\mathrm{d}r^2} + r\frac{\mathrm{d}\widehat{\psi}}{\mathrm{d}r} - \left(\mu^2 r^2 + 1\right)\widehat{\psi} = \frac{gr^2}{c_p T_0 N^2}\frac{\mathrm{d}\widehat{Q}}{\mathrm{d}r}, \tag{7}$$

$$\frac{\partial \widehat{T}}{\partial t} = \frac{\widehat{Q}}{c_p} - \frac{T_0 N^2}{g}\widehat{w}, \tag{8}$$

where

$$\mu(r) = \left\{\frac{\widehat{f}(r)}{N}\right\}\left\{\left(\frac{\pi}{z_{\mathrm{T}}}\right)^2 + \left(\frac{1}{2H}\right)^2\right\}^{1/2}$$

is the inverse Rossby length, and $\widehat{w} = \mathrm{d}(r\widehat{\psi})/r\mathrm{d}r$. Thus, the original task of solving the partial differential equation (2) for $\psi(r, z)$ and using the result in (6) to obtain $\partial T/\partial t$ has been simplified to the task of solving the ordinary differential equation (7) for $\widehat{\psi}(r)$ and using the result in (8) to obtain $\partial \widehat{T}/\partial t$. Under certain instances, a storm's vertical profile of latent heating may deviate slightly from the assumed structure above and it may be of interest to examine more closely the impact of heating that includes higher-order vertical internal modes in future research.

It is the relationship between the radial distribution of $\mu(r)$ and the transverse circulation

$$(u, w) = \left(-\mathrm{e}^{z/H}\frac{\partial \psi}{\partial z},\ \mathrm{e}^{z/H}\frac{\partial (r\psi)}{r\partial r}\right)$$

Copyright © 2008 Royal Meteorological Society

DOI: 10.1002/qj

that we are interested in exploring. To treat radial variations of $\mu(r)$ in a simple manner, we consider the specific barotropic vortex in which the square of the absolute angular momentum is given by

$$m^2(r) = \left\{ rv(r) + \frac{1}{2} f r^2 \right\}^2 = \left\{ r_j v(r_j) + \frac{1}{2} f r_j^2 \right\}^2 + \frac{1}{4} \widehat{f}_j^2 (r^4 - r_j^4) \quad \text{for} \quad r_j \le r \le r_{j+1}.$$

Here we consider a five-region model ($j = 0, 1, 2, 3, 4$) with $r_0 = 0$ denoting the origin, r_1 and r_2 denoting the bounding radii of the inner eyewall, r_3 and r_4 denoting the bounding radii of the outer eyewall, and $r_5 = \infty$. The five specified constants $\widehat{f}_j$ ($j = 0, 1, 2, 3, 4$) give the effective Coriolis parameters in the five regions. The five-region analysis presented here is a generalization of the 3-region (eye, eyewall, far-field) analysis described by Schubert *et al.* (2007). The goal of the more complicated five-region model (eye, inner eyewall, moat, outer eyewall, far-field) is to understand certain balanced dynamical aspects of the concentric eyewall phenomenon. Since, for each interval $r_j < r < r_{j+1}$,

$$\widehat{f}(r) = \left(\frac{\partial m^2}{r^3 \, \partial r} \right)^{1/2} = \left[\left\{ f + \frac{2v}{r} \right\} \left\{ f + \frac{\partial (rv)}{r \partial r} \right\} \right]^{1/2} = \widehat{f}_j, \tag{9}$$

the inverse Rossby length has the piecewise constant form

$$\mu(r) = \begin{cases} \mu_0 & \text{if } 0 \le r < r_1 \text{ (eye)}, \\ \mu_1 & \text{if } r_1 \le r < r_2 \text{ (inner eyewall)}, \\ \mu_2 & \text{if } r_2 \le r < r_3 \text{ (moat)}, \\ \mu_3 & \text{if } r_3 \le r < r_4 \text{ (outer eyewall)}, \\ \mu_4 & \text{if } r_4 \le r < \infty \text{ (far-field)}, \end{cases} \tag{10}$$

$$\text{where} \quad \mu_j = \frac{\widehat{f}_j}{N} \left\{ \left(\frac{\pi}{z_{\mathrm{T}}} \right)^2 + \left(\frac{1}{2H} \right)^2 \right\}^{1/2} \quad \text{for} \quad j = 0, 1, 2, 3, 4.$$

We now assume that the diabatic heating occurs in concentric eyewalls, with the particular piecewise constant form

$$\widehat{Q}(r) = \begin{cases} 0 & \text{if } 0 \le r < r_1 \text{ (eye)}, \\ Q_1 & \text{if } r_1 \le r < r_2 \text{ (inner eyewall)}, \\ 0 & \text{if } r_2 \le r < r_3 \text{ (moat)}, \\ Q_3 & \text{if } r_3 \le r < r_4 \text{ (outer eyewall)}, \\ 0 & \text{if } r_4 \le r < \infty \text{ (far-field)}, \end{cases} \tag{11}$$

where Q_1 and Q_3 are constants. Only five of the six constants $r_1, r_2, r_3, r_4, Q_1, Q_3$ are independently specified. The six constants are constrained by the assumption that

$$2 \int_0^\infty \left(\frac{\widehat{Q}}{c_p} \right) r \, \mathrm{d}r = \left(\frac{Q_1}{c_p} \right) (r_2^2 - r_1^2) + \left(\frac{Q_3}{c_p} \right) (r_4^2 - r_3^2) = 125 \text{ K day}^{-1} (50 \text{ km})^2. \tag{12}$$

A rough interpretation of this constraint is that the implied, area-averaged rainfall is fixed as we vary any five of the six parameters $r_1, r_2, r_3, r_4, Q_1, Q_3$. The particular values chosen in the last equality in (12) are motivated by satellite-derived observations during convectively active phases in an intense tropical cyclone (e.g. Rodgers *et al.*, 1998). Nonetheless, it should be noted that the exact value of latent heating on the right-hand side of (12) is not important to our radial structure arguments since (2) and (7) are linear equations for the streamfunction.

The jump conditions, derived by integrating (7) across narrow intervals straddling the points $r = r_1, r_2, r_3, r_4$, are

$$[\widehat{w}]_{r_j-}^{r_j+} = \left[\frac{\mathrm{d}(r\widehat{\psi})}{r \, \mathrm{d}r} \right]_{r_j-}^{r_j+} = \frac{g\{\widehat{Q}(r_j+) - \widehat{Q}(r_j-)\}}{c_p T_0 N^2}, \tag{13}$$

for $j = 1, 2, 3, 4$. Note that these jump conditions, when used in (8), result in the continuity of $\partial \widehat{T} / \partial t$ across r_j.

Under the assumptions (10) and (11), the solution of the ordinary differential equation (7) consists of linear combinations of the modified Bessel functions $I_1(\mu r)$ and $K_1(\mu r)$ in each of the five regions. Because $\widehat{\psi} = 0$ at $r = 0$, we can discard the $K_1(\mu r)$ solution in the inner region. Similarly, because $r\widehat{\psi} \to 0$ as $r \to \infty$, we can discard the $I_1(\mu r)$ solution in the outer region. The solution of (7) can then be written as

$$\widehat{\psi}(r) = \begin{cases} \widehat{\psi}_1 I_1(\mu_0 r)/I_1(\mu_0 r_1) \\ \{\widehat{\psi}_1 F_1(r, r_2) + \widehat{\psi}_2 F_1(r_1, r)\}/F_1(r_1, r_2) \\ \{\widehat{\psi}_2 F_2(r, r_3) + \widehat{\psi}_3 F_2(r_2, r)\}/F_2(r_2, r_3) \\ \{\widehat{\psi}_3 F_3(r, r_4) + \widehat{\psi}_4 F_3(r_3, r)\}/F_3(r_3, r_4) \\ \widehat{\psi}_4 K_1(\mu_4 r)/K_1(\mu_4 r_4), \end{cases} \tag{14}$$

where $F_j(x, y) = I_1(\mu_j x) K_1(\mu_j y) - K_1(\mu_j x) I_1(\mu_j y)$ for $j = 1, 2, 3$, and $\widehat{\psi}_1$, $\widehat{\psi}_2$, $\widehat{\psi}_3$, $\widehat{\psi}_4$ are constants to be determined by the four jump conditions (13). In (14), as well as below in (15), the five lines on the right-hand side (proceeding from top to bottom) give the solution in the eye, inner eyewall, moat, outer eyewall, and far-field. Note that the continuity of $\widehat{\psi}(r)$ at $r = r_1, r_2, r_3, r_4$ directly follows from the fact that the function $F_j(x, y)$ vanishes when its two arguments are equal. Using

$$\widehat{w} = \frac{1}{r} \frac{\mathrm{d}(r\widehat{\psi})}{\mathrm{d}r}$$

Copyright © 2008 Royal Meteorological Society

DOI: 10.1002/qj

and the derivative relations

$$\frac{1}{r}\frac{\mathrm{d}\{rI_1(\mu r)\}}{\mathrm{d}r} = \mu I_0(\mu r)$$
$$\text{and } \frac{1}{r}\frac{\mathrm{d}\{rK_1(\mu r)\}}{\mathrm{d}r} = -\mu K_0(\mu r),$$

it immediately follows that

$$\widehat{w}(r) = \begin{cases} \mu_0\widehat{\psi}_1 I_0(\mu_0 r)/I_1(\mu_0 r_1) \\ \mu_1\{\widehat{\psi}_1 G_1(r,r_2) - \widehat{\psi}_2 G_1(r,r_1)\}/F_1(r_1,r_2) \\ \mu_2\{\widehat{\psi}_2 G_2(r,r_3) - \widehat{\psi}_3 G_2(r,r_2)\}/F_2(r_2,r_3) \\ \mu_3\{\widehat{\psi}_3 G_3(r,r_4) - \widehat{\psi}_4 G_3(r,r_3)\}/F_3(r_3,r_4) \\ -\mu_4\widehat{\psi}_4 K_0(\mu_4 r)/K_1(\mu_4 r_4), \end{cases} \tag{15}$$

where $G_j(x,y) = I_0(\mu_j x)K_1(\mu_j y) + K_0(\mu_j x)I_1(\mu_j y)$ for $j = 1, 2, 3$. Use of (15) in the jump conditions (13) leads to four algebraic equations that determine $\widehat{\psi}_1, \widehat{\psi}_2, \widehat{\psi}_3, \widehat{\psi}_4$. With the aid of the Wronskian $I_0(x)K_1(x) + K_0(x)I_1(x) = 1/x$ we can write the four algebraic equations for $\widehat{\psi}_1, \widehat{\psi}_2, \widehat{\psi}_3, \widehat{\psi}_4$ as

$$\begin{pmatrix} a_{11} & a_{12} & 0 & 0 \\ a_{21} & a_{22} & a_{23} & 0 \\ 0 & a_{32} & a_{33} & a_{34} \\ 0 & 0 & a_{43} & a_{44} \end{pmatrix} \begin{pmatrix} \widehat{\psi}_1 \\ \widehat{\psi}_2 \\ \widehat{\psi}_3 \\ \widehat{\psi}_4 \end{pmatrix} = \frac{g}{c_p T_0 N^2} \begin{pmatrix} r_1 Q_1 \\ -r_2 Q_1 \\ r_3 Q_3 \\ -r_4 Q_3 \end{pmatrix}, \tag{16}$$

where

$$\begin{aligned} a_{11} &= \frac{\mu_1 r_1 G_1(r_1,r_2)}{F_1(r_1,r_2)} - \frac{\mu_0 r_1 I_0(\mu_0 r_1)}{I_1(\mu_0 r_1)}, \\ a_{22} &= \frac{\mu_1 r_2 G_1(r_2,r_1)}{F_1(r_1,r_2)} + \frac{\mu_2 r_2 G_2(r_2,r_3)}{F_2(r_2,r_3)}, \\ a_{33} &= \frac{\mu_2 r_3 G_2(r_3,r_2)}{F_2(r_2,r_3)} + \frac{\mu_3 r_3 G_3(r_3,r_4)}{F_3(r_3,r_4)}, \\ a_{44} &= \frac{\mu_3 r_4 G_3(r_4,r_3)}{F_3(r_3,r_4)} - \frac{\mu_4 r_4 K_0(\mu_4 r_4)}{K_1(\mu_4 r_4)}, \\ a_{12} &= a_{21} = -\frac{1}{F_1(r_1,r_2)}, \\ a_{23} &= a_{32} = -\frac{1}{F_2(r_2,r_3)}, \\ a_{34} &= a_{43} = -\frac{1}{F_3(r_3,r_4)}. \end{aligned} \tag{17}$$

The procedure for calculating $\widehat{w}(r)$ and $\partial\widehat{T}(r)/\partial t$ can be summarized as follows:

(i) Specify the vortex parameters $r_1, r_2, r_3, r_4, \mu_0, \mu_1, \mu_2, \mu_3, \mu_4$;
(ii) Specify one of the heating parameters Q_1 or Q_3, and determine the other through the constraint (12);

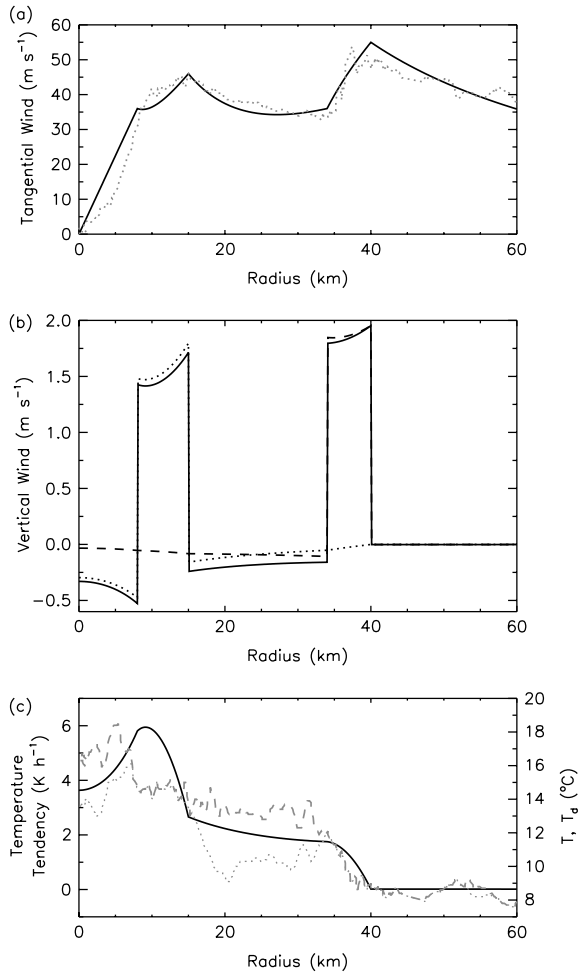

Figure 3. (a) Observed (dotted) and idealized (solid) tangential wind $v(r)$ (m s^{-1}) profiles at 700 hPa for *Frances* between 2117 and 2126 UTC on 30 August 2004. (b) Radially dependent part of log-pressure vertical velocity $\widehat{w}(r)$ (m s^{-1}), given by (15), due to the inner eyewall ($\widehat{w}_{\text{inner}}$, dotted), the outer eyewall ($\widehat{w}_{\text{outer}}$, dashed), and total vertical motion ($\widehat{w}$, solid). (c) Observed temperature (°C, dashed), observed dewpoint temperature (°C, dotted), and the radially dependent part of the temperature tendency $\partial\widehat{T}(r)/\partial t$ (K h^{-1}, solid) given by (8).

(iii) Solve the linear algebraic system (16) for $\widehat{\psi}_1, \widehat{\psi}_2, \widehat{\psi}_3, \widehat{\psi}_4$;
(iv) Compute $\widehat{w}(r)$ from (15) and $\partial\widehat{T}(r)/\partial t$ from (8).

4. Prototype concentric eyewalls

From the five-region analytical model we can learn more about the secondary circulation in different concentric eyewall situations. As a prototypical example, we now revisit the hurricane *Frances* situation on 30 August 2004. The dotted line in Figure 3(a) shows the 700 hPa tangential wind data from the period 2117–2126 UTC (cf. Figure 2(f)). To approximate this observed case, we choose:

$f = 5 \times 10^{-5}$ s^{-1}, $H = RT_0/g = 8.79$ km,
$(N/f)\{(\pi/z_{\mathrm{T}})^2 + (2H)^{-2}\}^{-1/2} = 1000$ km,
$N = 1 \times 10^{-2}$ s^{-1}, $(r_1, r_2, r_3, r_4) = (8, 15, 34, 40)$ km

Copyright © 2008 Royal Meteorological Society

DOI: 10.1002/qj

and $(v(r_1), v(r_2), v(r_3), v(r_4)) = (36, 46, 36, 55)$ m s^{-1}, which results in $(\mu_0^{-1}, \mu_1^{-1}, \mu_2^{-1}, \mu_3^{-1}, \mu_4^{-1}) = (5.5, 8.5, 27.2, 14.9, 1000)$ km. This five-region approximation to the observed tangential wind profile is shown by the solid line in Figure 3(a). As for the forcing, we choose $Q_1 = Q_3$ and then enforce the constraint (12), which yields $Q_1/c_p = Q_3/c_p = 21.5$ K h^{-1}.

The $\widehat{w}(r)$ profile, computed from (15), is shown in Figure 3(b) (solid curve), and the corresponding $\partial\widehat{T}(r)/\partial t$ profile, computed from (8), is shown in Figure 3(c) (solid curve). There is upward motion of magnitude 1.4 to 2.0 m s^{-1} in the inner and outer eyewall regions, with strongest subsidence in the eye and weakest subsidence in the far-field. The eye radius ($r_1 = 8$ km) is larger than the Rossby length in the eye ($\mu_0^{-1} = 5.5$ km). Under these conditions there is considerable horizontal variation of subsidence in the eye, with the strongest subsidence at the outer edge of the eye (Schubert *et al.*, 2007). In contrast, the width of the moat ($r_3 - r_2 = 19$ km) is smaller than the Rossby length in the moat ($\mu_2^{-1} = 27.2$ km), so that there is less horizontal variation of subsidence in the moat. The magnitude of subsidence in the moat varies between 0.20 and 0.25 m s^{-1}. These values of subsidence are sufficient to produce temperature tendencies (solid curve in Figure 3(c)) of approximately 2 K h^{-1} within the moat. Although the diabatic heating is equal in the inner and outer eyewalls, the temperature tendency is larger in the inner region because the Rossby lengths are smaller there. Also shown in Figure 3(c) are the observed 700 hPa radial profiles of temperature and dewpoint temperature. Note that the theoretical $\partial\widehat{T}(r)/\partial t$ profile has a radial structure similar to the observed temperature profile, although the peak in the theoretical $\partial\widehat{T}(r)/\partial t$ profile lies outside the peak in the observed temperature. Regions of large dewpoint depression, a telltale sign of subsidence, are found in the eye and the moat.

Although the example shown in Figure 3 is typical of many concentric eyewall configurations, there are cases with much wider moats. For example, in the case of typhoon *Winnie* (1997) the moat was approximately 130 km wide (Lander, 1999; Zhang *et al.*, 2005). In cases with such wide moats or with large vorticity in the moat, the Rossby length in the moat can be smaller than the moat width, in which case there will be large horizontal variation of subsidence across the moat.

Why does the inner eyewall often disappear? Possible mechanisms include:

(i) Each eyewall has a suppressing effect on the other through the subsidence it induces in its surroundings, but the outer eyewall somehow has a competitive advantage in this regard;
(ii) Concentric eyewalls interact through the boundary layer in such a way that the outer eyewall consumes the inward radial flux of moist entropy and momentum, effectively choking off convection and higher vorticity in the inner eyewall;
(iii) Since the storm's upper tropospheric warm core weakens with radius, it more effectively limits inner eyewall convection through increased static stability, a process that leads to the decay of the inner eyewall and the growth of the outer eyewall;
(iv) On a similar note, a developing concentric eyewall will decrease the convective instability at radii inside the outer eyewall due to increased subsidence warming and drying.

Although our idealized model does not contain enough physics to critically evaluate all of these possible explanations, it does provide useful information. For example, we can readily address mechanism (i) in the following way. Since the transverse circulation equation is linear, the total solution shown in Figure 3(b) can be interpreted as the superposition of two solutions, i.e. $\widehat{w}(r) = \widehat{w}_{\text{inner}}(r) + \widehat{w}_{\text{outer}}(r)$. The $\widehat{w}_{\text{inner}}(r)$ field is obtained from (15) with $\widehat{\psi}_1, \widehat{\psi}_2, \widehat{\psi}_3, \widehat{\psi}_4$ determined from (16) as before but now with $Q_3 = 0$. Similarly, $\widehat{w}_{\text{outer}}(r)$ is obtained from (15) with $\widehat{\psi}_1, \widehat{\psi}_2, \widehat{\psi}_3, \widehat{\psi}_4$ determined from (16) as before but now with $Q_1 = 0$. In other words, $\widehat{w}_{\text{inner}}(r)$ is the vertical motion field that would exist for the same vortex structure if the diabatic heating associated with the outer eyewall was not present, while $\widehat{w}_{\text{outer}}(r)$ is the vertical motion field that would exist if the diabatic heating associated with the inner eyewall was not present. Radial profiles of $\widehat{w}_{\text{inner}}(r)$ and $\widehat{w}_{\text{outer}}(r)$ are displayed in Figure 3(b), which shows that subsidence in the eye is almost entirely due to diabatic heating in the inner eyewall, while subsidence near the centre of the moat is due equally to diabatic heating in the inner and outer eyewalls. From Figure 3(b) it is also apparent that each eyewall has the effect of suppressing the other, but that the effect is essentially mutual and quite small. Thus, the first mechanism does not appear to be a good candidate for explaining the disappearance of the inner eyewall.

In the following two sections, we address aspects of hypotheses (iii) and (iv) by examining the impact of the varying diabatic heating and inertial stability associated with a developing concentric eyewall. First, we demonstrate that, as diabatic heating shifts from an inner eyewall to an outer eyewall, the tropical cyclone loses its ability to maintain a strong, centralized warm core. Then, considering a hypothetical eyewall replacement cycle, we find that the downward mass flux within the moat increases rapidly as an outer eyewall strengthens and contracts. The increased inertial stability associated with this process greatly increases the temperature tendency within the core of the tropical cyclone.

5. The decrease of inner core temperature change associated with the collapse of inner eyewall convection

As an idealization of a collapsing inner eyewall during an eyewall replacement cycle, we again consider the tangential wind profile given in Figure 3(a), but now consider the three diabatic heating profiles given in

Copyright © 2008 Royal Meteorological Society

DOI: 10.1002/qj

Figure 4(a). All three of these diabatic heating profiles satisfy the total heating constraint (12). The dotted profile ($Q_1/Q_3 = 2$) represents an early stage of inner eyewall dominance, the dashed profile ($Q_1/Q_3 = 1$) represents an intermediate stage, and the solid profile ($Q_1/Q_3 = 0.5$) is near the final stage of inner eyewall collapse. Figure 4(b) shows the temperature tendencies associated with these three diabatic heating profiles. When the diabatic heating rate in the inner eyewall is large, the local temperature tendency is concentrated near $r = 9$ km. However, as the diabatic heating shifts from the inner eyewall to the outer eyewall, the tropical cyclone loses its ability to produce an intense, highly localized warm region.

To further quantify this important effect, we now define the 'core' as the region that includes the eye, the inner eyewall, the moat, and the outer eyewall, i.e. as the region $0 \le r \le r_4$. Integrating (8) over the core, we obtain

$$\int_0^{r_4} (\partial \widehat{T}/\partial t)\, r\, \mathrm{d}r = \int_0^{r_4} (\widehat{Q}/c_p)\, r\, \mathrm{d}r - \left(\frac{T_0}{g}\right) N^2 r_4 \widehat{\psi}_4. \tag{18}$$

Similarly, integrating (8) over the entire domain, we obtain

$$\int_0^{\infty} (\partial \widehat{T}/\partial t)\, r\, \mathrm{d}r = \int_0^{\infty} (\widehat{Q}/c_p)\, r\, \mathrm{d}r = \frac{1}{2} 125 \text{ K day}^{-1} (50 \text{ km})^2, \tag{19}$$

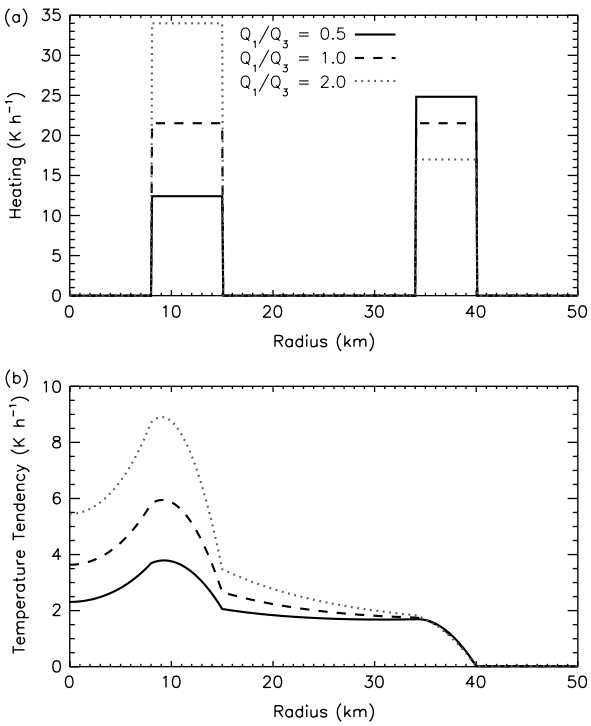

Figure 4. (a) Idealized radial profiles of the diabatic heating during the collapse of the inner eyewall. The dotted line ($Q_1/Q_3 = 2$) is the early stage, the dashed line ($Q_1/Q_3 = 1$) is an intermediate stage, and the solid line ($Q_1/Q_3 = 0.5$) is the final stage of collapse. (b) Corresponding radial profiles of $\partial \widehat{T}/\partial t$, computed from (8).

where the last equality follows from (12). Equation (19) states that the area-integrated temperature change equals the area-integrated diabatic heating, which we have assumed is fixed according to (12). As can be seen from (18), although the total diabatic heating occurs entirely within the core, the temperature change is partitioned between the core and the far-field according to the value of $r_4 \widehat{\psi}_4$. Dividing (18) by (19) we obtain

$$\epsilon = \int_0^{r_4} \left(\frac{\partial \widehat{T}}{\partial t}\right) r\, \mathrm{d}r \Bigg/ \int_0^{\infty} \left(\frac{\partial \widehat{T}}{\partial t}\right) r\, \mathrm{d}r = 1 - \frac{(T_0/g) N^2 2 r_4 \widehat{\psi}_4}{(Q_1/c_p)(r_2^2 - r_1^2) + (Q_3/c_p)(r_4^2 - r_3^2)}, \tag{20}$$

an expression for the fraction of total diabatic heating used to increase the temperature of the core. Of particular interest here is how ϵ changes as the diabatic heating shifts from the inner eyewall to the outer eyewall during an eyewall replacement cycle. For $Q_1/Q_3 = 2.0$, 1.0, 0.5, the respective values are $\epsilon =$ 32.7%, 26.4%, 21.8%. Note that, as $\partial \widehat{T}/\partial t$ becomes smaller in the core, it must become larger in the far-field in order to satisfy (19). However, this change of $\partial \widehat{T}/\partial t$ in the far-field is imperceptible in Figure 4(b) because of the large area over which it is spread.

6. Changes in the transverse circulation during contraction of an outer eyewall

Next, we are interested in determining the impact of a contracting and intensifying outer eyewall on the vertical motion and temperature change in the storm's core. We idealize this part of the eyewall cycle by setting $r_1 =$ 8 km, $r_2 = 15$ km, $v(r_1) = 36$ m s^{-1}, $v(r_2) = 46$ m s^{-1}, and then letting r_4 decrease from 85 km to 40 km while keeping $r_4 - r_3 = 6$ km, fixing Q_1 according to the prototype concentric eyewalls in Section 4, and setting Q_3 to satisfy constraint (12). Three selected $v(r)$ profiles are shown in Figure 5(a). The corresponding values of r_3, r_4, $v(r_3)$, $v(r_4)$, μ_2^{-1}, μ_3^{-1} are given in Table I. All three profiles have $\mu_0^{-1} = 5.5$ km, $\mu_1^{-1} = 8.5$ km and $\mu_4^{-1} = 1000$ km, but, as can be seen in Table I, the Rossby length in the moat decreases from $\mu_2^{-1} =$ 1000 km to $\mu_2^{-1} = 27.2$ km while the Rossby length in the outer eyewall decreases from $\mu_3^{-1} = 1000$ km to $\mu_3^{-1} = 14.9$ km. This idealized outer eyewall contraction is in general agreement with the eyewall replacement cycle described earlier for hurricane *Frances*.

The fields of $\widehat{w}$ and $\partial \widehat{T}/\partial t$ are shown in Figures 5(b,c). These results show that, as the outer eyewall moves inward, the subsidence rates within the moat and eye both increase by up to -0.25 m s^{-1}. Because the Rossby lengths in the moat and outer eyewall decrease substantially during this transition (Table I), radial variations of $\widehat{w}(r)$ increase within these regions. While the fractional change in upward motion in the primary eyewall decreases slightly during the eyewall replacement cycle,

Copyright © 2008 Royal Meteorological Society

DOI: 10.1002/qj

Table I. Bounding radii of the outer eyewall, r_3 and r_4, zimuthal winds $v(r_3)$ and $v(r_4)$, and Rossby lengths in the moat, μ_2^{-1}, and the outer eyewall, μ_3^{-1}, for the wind profiles shown in Figure 5.

Case	r_3 (km)	r_4 (km)	$v(r_3)$ (m s^{-1})	$v(r_4)$ (m s^{-1})	μ_2^{-1} (km)	μ_3^{-1} (km)
A	79	85	7.0	6.3	1000	1000
B	56	62	21.5	30.7	72.8	36.5
C	34	40	36.0	55.0	27.2	14.9

the fractional changes of subsidence within the moat and eye are significant. Within the core (i.e. $0 \le r \le r_4$), there is an increase in $\partial\widehat{T}/\partial t$ associated with the enhanced subsidence (Figure 5(c)). The change in $\partial\widehat{T}/\partial t$ is increasingly enhanced throughout the core as the outer eyewall moves inward and strengthens.

Another way to gauge the impact of a contracting outer eyewall on subsidence is to calculate the percentage of the total downward mass flux occurring in the eye, the moat, and the far-field. We define σ_{eye}, σ_{moat}, and $\sigma_{\text{far-field}}$ as the fractions of the total downward mass flux that occur respectively in the eye, moat, and far-field. From the streamfunction solution (14) it can be shown that, on any isobaric surface,

$$\sigma_{\text{eye}} = \frac{r_1\widehat{\psi}_1}{r_1\widehat{\psi}_1 + r_3\widehat{\psi}_3 - r_2\widehat{\psi}_2 - r_4\widehat{\psi}_4},$$
$$\sigma_{\text{moat}} = \frac{r_3\widehat{\psi}_3 - r_2\widehat{\psi}_2}{r_1\widehat{\psi}_1 + r_3\widehat{\psi}_3 - r_2\widehat{\psi}_2 - r_4\widehat{\psi}_4},$$
$$\sigma_{\text{far-field}} = 1 - \sigma_{\text{eye}} - \sigma_{\text{moat}}. \tag{21}$$

Using (21), σ_{eye}, σ_{moat}, and $\sigma_{\text{far-field}}$ can be obtained from the solutions of the linear algebra problem (16). Note that the downward mass flux partition does not depend on the magnitude of heating in (11), but rather on the radial structure of heating.

Figure 6 shows profiles of σ_{moat} and σ_{eye} for two different experiments. The control experiment (Exp. 1) is described above as the basic, idealized eyewall replacement cycle. Exp. 2 is identical to Exp. 1 except that the tangential wind profile is not changed during the contraction of the outer eyewall, i.e. the tangential wind profile is held fixed to that shown by Profile A in Figure 5(a). A comparison of these two experiments (Figure 6) isolates the effect of the changing inertial stability (present in Exp. 1 but not in Exp. 2) during outer eyewall contraction. In Exp. 1 the fraction of downward mass flux in the moat increases quickly from about 1% to 16%. In addition, contraction of the outer eyewall also increases the fraction of downward mass flux in the eye from 7% to 11%. In contrast, a slight decrease in the downward mass flux in the moat and eye are experienced in Exp. 2, even though the outer ring of diabatic heating contracts inward toward the inner eyewall. Therefore, we conclude that the increasing inertial stability associated

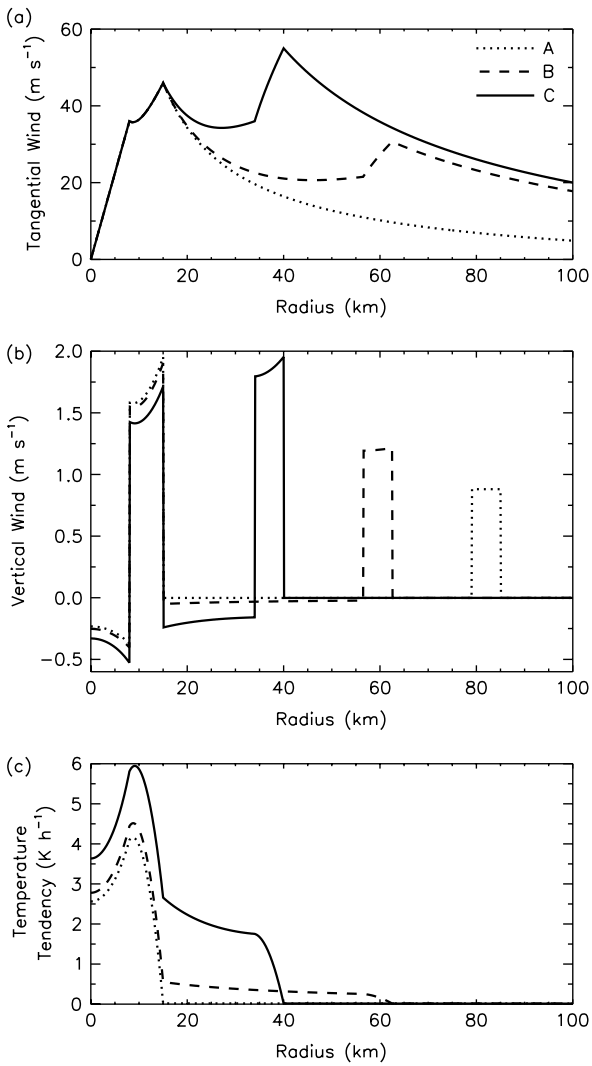

Figure 5. Radial profiles of (a) tangential wind (m s^{-1}), (b) the radially dependent part of the log-pressure vertical velocity $\widehat{w}(r)$ (m s^{-1}) computed from (15), and (c) the radially dependent part of the temperature tendency $\partial\widehat{T}(r)/\partial t$ (K h^{-1}), computed from (8), for cases A (dotted), B (dashed), and C (solid).

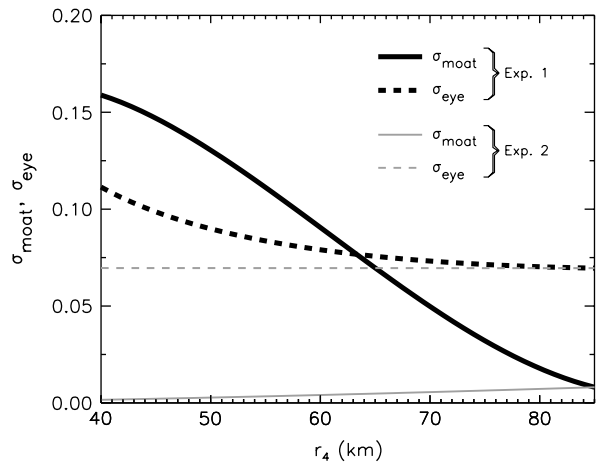

Figure 6. Values of the fraction of downward mass flux in the moat, σ_{moat} (solid), and the fraction of downward mass flux in the eye, σ_{eye} (dotted), for the range of wind profiles shown in Figure 5. The abscissa denotes the variable parameter r_4. Black and grey curves denote results from Exp. 1 and Exp. 2, respectively.

Copyright © 2008 Royal Meteorological Society

DOI: 10.1002/qj

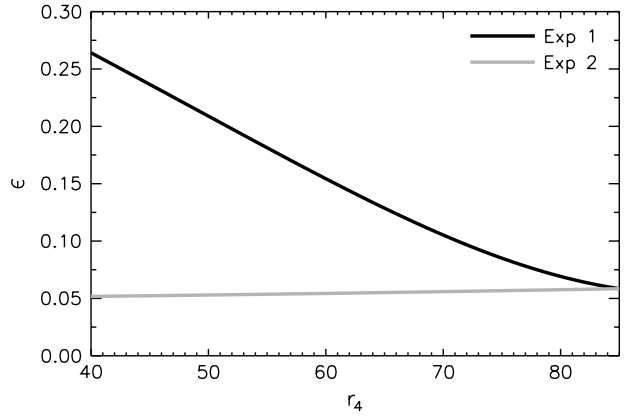

Figure 7. Values of the fraction of total diabatic heating used to increase the temperature of the core, as given in (20), for the range of wind profiles shown in Figure 5, from Exp. 1 (black) and Exp. 2 (grey).

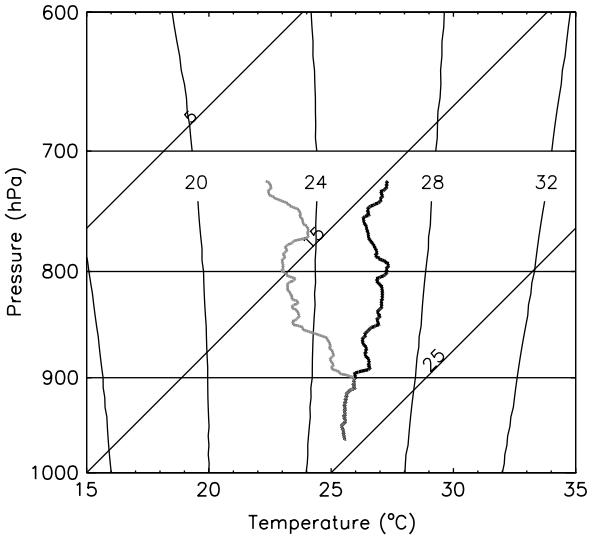

Figure 8. A skew$T$–log p diagram of dropsonde data at $r = 24$ km in hurricane *Frances* at 1810 UTC on 30 August 2004. Temperature (°C) and dewpoint (°C) are given by the black and grey curves. Data obtained courtesy of NOAA/HRD.

with a strengthening outer eyewall is an essential factor controlling subsidence within the moat.

To complement the downward mass flux calculations, Figure 7 presents the fraction of total diabatic heating used to increase the temperature of the core, as given in (20), for the range of wind profiles depicted in Figure 5. Not surprisingly, very little change in ϵ is seen for Exp. 2. However, including the increasing inertial stability associated with the contraction of the outer eyewall changes the core heating fraction dramatically from about 5% to 27%. In agreement with results presented by Schubert and Hack (1982), the ability of the storm to build its warm core increases dramatically with increasing inertial stability associated with a strengthening outer eyewall. In terms of efficiently building a warm core, a contracting and intensifying outer eyewall counteracts the deleterious impact of shifting heating from the inner to outer eyewall. Furthermore, these results suggest that the development of deep, convective clouds in the moat, and most likely within the inner eyewall, will become increasingly challenged by increasing static stability as temperature tendencies increase with increasing inertial stability.

Houze *et al.* (2007) presented dropsonde data in the eye and moat of hurricane *Rita* (2005). Their soundings reveal how the moat gradually takes on the characteristics of the eye. Dropsonde data in *Frances* reveal a similar evolution. For example, Figure 8 shows dropsonde data taken on the leg A → B (Figure 2(a)) at a radius 24 km west of the centre. Although this sounding is in the moat, it has the basic characteristics of an eye sounding, i.e. saturation in a stratocumulus layer below 900 hPa, with increased stability and drying above 900 hPa. Our 5-region model suggests that the downward mass flux and the associated warming in the moat increases dramatically as a concentric eyewall begins to form and contract. Therefore, in an axisymmetric, balanced tropical cyclone vortex with concentric eyewalls, eye-like conditions in the moat are not surprising.

7. Conclusions

In summary, we have investigated the analytical solutions of a transverse circulation equation derived from a balanced vortex model to explore motions associated with a barotropic tropical cyclone vortex. This idealized vortex was parametrized with two concentric rings of diabatic heating and five regions of potentially distinct inertial stability values that approximate realistic tropical cyclone tangential wind profiles. Flight-level wind data from hurricane *Frances* (2004) were used to parametrize our five-region model. The resulting radial distribution of diagnosed vertical motion shows enhanced subsidence within the eye and the moat. The corresponding radial structure of temperature tendencies resembles the warm core radial profile of observed, flight-level temperatures. Thus, the eye-like conditions observed within the mature moat of *Frances* are consistent with the quasi-balanced dynamics.

We have argued against the hypothesis that the inner eyewall tends to collapse because of the suppressive effect of the subsidence induced by the outer eyewall. Because our simple model does not contain a frictional planetary boundary layer, we cannot adequately address the impact of concentric eyewalls on low-level inflow and its associated radial moist entropy flux. However, the transverse circulation equation quantitatively confirms previous claims that a contracting and intensifying outer eyewall increases subsidence within the moat and eye. Moat subsidence contains comparable contributions from both eyewalls and most of this subsidence results from enhanced inertial stability associated with a strengthening outer eyewall. During an eyewall replacement cycle, warming of the core increases in response to enhanced core subsidence. Assuming that surface temperatures are approximately constant, rapidly increasing static stability within the core can be expected during the progression of an eyewall replacement cycle, which is expected

Copyright © 2008 Royal Meteorological Society

DOI: 10.1002/qj

to challenge any deep convective clouds at any radius inside the outer eyewall. While a contracting and intensifying outer eyewall increases the warming rates within the storm's core, we expect a counteracting feedback to occur as diabatic heating shifts from an inner eyewall to an outer eyewall. Thus, the balanced dynamics offer a partial explanation of how an eyewall replacement cycle can serve as a temporary brake on tropical cyclone intensification.

It is natural to ponder whether the balanced vortex model provides any insights into the challenging forecast problem of concentric eyewall formation. First, this model is very restricted by its neglect of asymmetries, which are hypothesized to play a critical role in secondary eyewall formation (e.g. Montgomery and Kallenbach, 1997; Kuo *et al*., 2004, 2008; Terwey and Montgomery, 2008). Nonetheless, this model suggests that once a secondary eyewall forms and begins to intensify, eye-like conditions rapidly develop within the moat. This implies that the role of rapid filamentation (e.g. Rozoff *et al*., 2006) becomes less relevant in explaining the absence of convection within the moat. However, rapid filamentation would enhance the deleterious impact of subsidence warming on convection within the moat and their joint impacts would aid in the development of well-defined concentric eyewalls.

One of the remaining hypotheses for the decay of the inner eyewall is that the upper-level warm core has a larger stabilization effect on the convection in the inner eyewall than it does on the convection in the outer eyewall. If this argument is correct, how does the outer eyewall later contract inward? Could the upper-level warm core relax, allowing convection to move inward? Our ability to answer these questions is hindered by a lack of upper-tropospheric data during concentric eyewall cycles. However, with the availability of the NOAA G-IV and the NASA ER-2 jet aircraft, both with dropsonde capability, a well-executed field programme might make important progress on this remaining problem in tropical cyclone dynamics. Finally, further analysis of three-dimensional, full-physics numerical simulations of intense tropical cyclones should further elucidate many physical mechanisms involved in eyewall replacement cycles and the decay of the primary eyewall. Nonetheless, our simplified approach helps delineate crucial physics in basic concentric eyewall situations.

Acknowledgements

We would like to thank Michael Black, Neil Dorst, Kevin Mallen, Brian McNoldy, Michael Montgomery, Dave Nolan, John Persing, Matthew Sitkowski, Wes Terwey and Jonathan Vigh for their comments and assistance. In addition, the insightful comments of two anonymous reviewers helped clarify aspects of this manuscript. This research was supported by NASA/TCSP grant 04-0007-0031, NSF grants ATM-0435694, ATM-0435644 and ATM-0332197, and ONR grant N00014-07-1-0163.

References

Eliassen A. 1951. Slow thermally or frictionally controlled meridional circulation in a circular vortex. *Astrophys. Norv.* **5**: 19–60.

Hausman SA. 2001. 'Formulation and sensitivity analysis of a nonhydrostatic, axisymmetric tropical cyclone model'. Department of Atmospheric Science Paper No. 701, Colorado State University.

Hawkins J, Helveston M, Lee TF, Turk FJ, Richardson K, Sampson C, Kent J, Wade R. 2006. 'Tropical cyclone multiple eyewall configurations'. Preprints, 27th Conference on Hurricanes and Tropical Meteorology, Monterey, CA. Amer. Meteorol. Soc: Boston.

Houze RA, Chen SS, Lee W-C, Rogers RF, Moore JA, Stossmeister GJ, Bell MM, Cetrone J, Zhao W, Rita Brodzik S. 2006. The Hurricane Rainband and Intensity Change Experiment: Observations and modeling of hurricanes Katrina, Ophelia, and Rita. *Bull. Am. Meteorol. Soc.* **87**: 1503–1521.

Houze RA, Chen SS, Smull BF, Lee W-C, Bell MM. 2007. Hurricane intensity and eyewall replacement. *Science* **315**: 1235–1239.

Kuo H-C, Lin L-Y, Chang C-P, Williams RT. 2004. The formation of concentric vorticity structures in typhoons. *J. Atmos. Sci.* **61**: 2722–2734.

Kuo H-C, Schubert WH, Tsai C-L, Kuo Y-F. 2008. Vortex interactions and barotropic aspects of concentric eyewall formation. *Mon. Weather Rev.* in press.

Lander MA. 1999. A tropical cyclone with a very large eye. *Mon. Weather Rev.* **127**: 137–142.

Montgomery MT, Kallenbach RJ. 1997. A theory for vortex Rossby waves and its application to spiral bands and intensity changes in hurricanes. *Q. J. R. Meteorol. Soc.* **123**: 435–465.

Rodgers EB, Olson WS, Karyampudi VM, Pierce HF. 1998. Satellite-derived latent heating distribution and environmental influences in hurricane Opal (1995). *Mon. Weather Rev.* **126**: 1229–1247.

Rozoff CM, Schubert WH, McNoldy BD, Kossin JP. 2006. Rapid filamentation zones in intense tropical cyclones. *J. Atmos. Sci.* **63**: 325–340.

Schubert WH, Hack JJ. 1982. Inertial stability and tropical cyclone development. *J. Atmos. Sci.* **39**: 1687–1697.

Schubert WH, Rozoff CM, Vigh JL, McNoldy BD, Kossin JP. 2007. On the distribution of subsidence in the hurricane eye. *Q. J. R. Meteorol. Soc.* **133**: 595–605.

Shapiro LJ, Willoughby HE. 1982. The response of balanced hurricanes to local sources of heat and momentum. *J. Atmos. Sci.* **39**: 378–394.

Terwey WD, Montgomery MT. 2008. Secondary eyewall formation in two idealized, full-physics modeled hurricanes. *J. Geophys. Res.* in press.

Willoughby HE, Black PG. 1996. Hurricane Andrew in Florida: Dynamics of a disaster. *Bull. Am. Meteorol. Soc.* **77**: 543–549.

Willoughby HE, Clos JA, Shoreibah MG. 1982. Concentric eyewalls, secondary wind maxima, and the evolution of the hurricane vortex. *J. Atmos. Sci.* **39**: 395–411.

Zhang Q-H, Kuo YH, Chen S-J. 2005. Interaction between concentric eye-walls in super typhoon *Winnie* (1997). *Q. J. R. Meteorol. Soc.* **131**: 3183–3204.

Copyright © 2008 Royal Meteorological Society

DOI: 10.1002/qj